

1000 - 10,000 M_{\odot} primordial stars created the nitrogen excess in the galaxy GS 3073 at $z = 5.55$

Authors: Devesh Nandal^{1*}, Daniel J. Whalen^{2*}, Muhammad A. Latif³, Alexander Heger⁴

Affiliations:

¹Department of Astronomy, University of Virginia, Charlottesville, VA 22904, USA.

*Corresponding author. Email: deveshnandal@yahoo.com, dwhalen1999@gmail.com

²Institute of Cosmology and Gravitation, University of Portsmouth; Portsmouth PO1 3FX, UK.

³Physics Department, College of Science, United Arab Emirates University; PO Box 15551, Al-Ain, UAE.

⁴School of Physics and Astronomy, Monash University, Vic. 3800, Australia

Abstract: The James Webb Space Telescope has revealed a wealth of new galaxies just a few hundred Myr after the Big Bang. Some of these galaxies exhibit unusual elemental abundances that are difficult to explain with stellar populations today. In particular, no known stars or supernovae can explain the N/O ratio of 0.46 in GS 3073 at redshift $z = 5.55$. Here we show that the extreme nitrogen abundances in GS 3073 can be produced by 1000 - 10,000 M_{\odot} Pop III stars. We find that these are the only stars that can also explain its C/O and Ne/O ratios. GS 3073 is thus the first conclusive evidence of the existence of supermassive Pop III stars at cosmic Dawn in the fossil abundance record.

Main Text: The James Webb Space Telescope has now revealed the existence of galaxies at redshifts $z \sim 14$, or 300 Myr after the big bang (1-6). Some of these galaxies exhibit N/O ratios that are difficult to explain with any known stellar population. Wolf-Rayet stars in multiple-burst populations (7), rapidly rotating primordial stars (8-9), general relativistic explosions of metal-enriched supermassive stars (10), or the precursors of globular clusters (11,12) in principle can account for the supersolar nitrogen excesses in the galaxies GN-z11 (13,14) and CEERS 1019 (15) but not those in GS 3073 at $z = 5.55$, which are far higher at $N/O = 0.46$ (16). However, primordial (or Pop III) stars of a few thousand solar masses (17-21) have recently been shown to produce large amounts of nitrogen late in their lives (22).

1000 - 10,000 M_{\odot} Pop III stars are thought to form in pristine, atomically-cooled gas in moderate Lyman-Werner (LW) UV flux from other stars (10 - 1000 J_{21} , $J_{21} = 10^{-21} \text{ erg s}^{-1} \text{ Hz}^{-1} \text{ sr}^{-1} \text{ cm}^{-2}$; 23,24). These less intense but more common LW fluxes prevented star formation in the gas until it began to be cooled primarily by $\text{Ly}\alpha$ emission but also by some H_2 (25). Hybrid $\text{Ly}\alpha$ / H_2 cooling caused collapse rates that were less than those in purely atomically-cooled gas (26-29) that formed $10^5 M_{\odot}$ stars, instead producing Pop III stars of $10^3 - 10^4 M_{\odot}$ (30). Such stars have long been held to be the seeds of the first quasars at $z > 6$ (31-33). We have now modeled the evolution of 1000 - 10,000 M_{\odot} Pop III stars in 1000 M_{\odot} (M_{\odot} , solar mass) increments with the Geneva Stellar Evolution Code (GENEC; 34) to determine if such stars can produce the extreme N/O ratio of GS 3073.

Results: We show the evolution of the 7000 M_{\odot} star as a fiducial case in the Hertzsprung-Russell (HR) and Kippenhahn diagrams in panels (a) and (b) of Fig. 1 and discuss its evolution in detail in the Supplementary Data. The other stars in our study exhibit similar histories. We list elemental yields for all ten stars in Supplementary Data Table 1 and discuss those for N, C, and Ne in detail below.

Elemental Yields

Abundance profiles for the 7000 M_{\odot} star at the end of Si burning are shown in Fig. 2. The thin radiative layer between the core and the convective H burning shell in panel (h) of Fig. 1 is permeable to products of nuclear burning, which pass into the H shell and fuse with hydrogen or are dispersed throughout the star. ^{12}C from He burning reaches the H shell at 1.22 Myr and fuses into ^{13}N and then ^{14}N . This channel creates the N excess consistent with that observed in GS 3073 because it continues throughout helium burning, the second longest evolutionary stage of the star. N is soon dispersed throughout the star by the numerous convective zones above the H layer, becoming the third most abundant element at the surface as shown Fig. S1. ^{16}O due to alpha captures by ^{12}C in the core, which can also create ^{14}N in the H shell, is also mixed throughout the star, becoming the fourth most abundant element at the surface.

^{14}N and ^{16}O synthesis via the CNO cycle depletes ^{12}C over time. Although it is the fourth most abundant element at the start of helium burning it falls to fifth place below ^{16}O by the middle as shown in Fig. S1. ^{14}N produced in the H shell also returns to the convective core and forms ^{22}Ne after the onset of He burning. This ^{22}Ne is then mixed throughout the star, becoming the sixth most abundant element at the surface. ^{16}O in the core from the CNO cycle can capture an alpha and form ^{20}Ne , but longer ^{16}O formation times result in less ^{20}Ne being produced than ^{22}Ne . Nuclear ash

created in the core after the end of central helium burning never reaches the outer layers of the star because convection timescales are longer than later stages of nuclear burning, which last just a few days. Heavier elements such as ^{26}Mg , ^{28}Si , ^{44}Ti , ^{48}Cr and ^{56}Ni thus remain trapped in the core, as shown in Fig. 2.

Abundance ratios / dilution factors

We calculate N/O, C/O, and Ne/O number ratios for comparison to those observed for GS 3073 with

$$\log \frac{\frac{M_X}{A_X}}{\frac{M_Y}{A_Y}} = \log \frac{M_X}{M_Y} + \log \frac{A_Y}{A_X}, \quad (1)$$

where the M and A are the masses in M_\odot and mass numbers of the elements, respectively. They are plotted versus mass coordinate for the 7000 M_\odot star at the end of Si burning in Fig. 3, in which the M used in Eq. 1 is the total mass of the given element lying above the mass coordinate. As discussed in the Supplementary Data, mass loss from these stars is likely but not well quantified, so we treat it as a free parameter and consider three fiducial values: 10% and 50% of the mass of the star and all the mass above its CO core. Thus, in Fig. 3 N/O = 1.175, C/O = -0.48 and O/H + 12 is 8.65 if 10% of the mass is ejected. The number ratios rise as the mass coordinate falls to 2050 M_\odot , the CO boundary, after which they diverge in the core because they depend on the evolutionary stage at which the element was created.

We parametrize enrichment of the galaxy by the star with a dilution factor defined to be the mass of the gas contaminated by ejecta from the star divided by the mass of the ejecta. We show N/O, C/O and Ne/O ratios measured against the O/H + 12 ratio for all 10 stars as a function of dilution factor from 1 - 1000 in the case of 10% mass loss in Fig. 4 and for 50% and CO mass loss in Figs. S2 and S3. The green star in all three figures marks the observed abundance ratio for GS 3073 derived from rest-frame UV emission lines (16). The yellow and brown stars are corresponding ratios for CEERS 1019 and GN-z11, high-redshift galaxies at $z = 8.68$ and 10.6 , respectively (11,12). Illumination by a Type-1 active galactic nucleus (AGN) in GS 3073, and its lower redshift, allow these ratios to be tightly constrained.

N/O ratios

For mass losses of 10% our stars produce N/O ratios higher than that of GS 3073 except for 9000 M_\odot , which has an N/O ratio of 0.39 at dilution factors of 20 - 30 that falls within the error bars for GS 3073. The second closest model is the 8000 M_\odot star, with an N/O ratio of 0.60 at dilution factors of 5 - 15. For mass losses of 50%, 8 of the 10 stars produce N/O ratios above those of GS 3073 except for the 9000 and 10,000 M_\odot models. The N/O ratios of the 8000 and 9000 M_\odot stars, 0.52 and 0.41, lie within the error bars for GS 3073 at dilution factors of 24 - 46. If the star sheds all its mass above the CO core only the 3000, 5000 and 7000 M_\odot stars produce N/O ratios greater than those of GS 3073. The others still exhibit relatively high N/O ratios, such as 0.1 for the 9000 M_\odot model. The 1000 and 3000 M_\odot stars closely match the observed abundances, with N/O ratios of 0.38 and 0.48 for dilution factors of 12 - 38 and 31 - 56, respectively.

C/O ratios

We show C/O ratios for all three mass losses in the top right panels of Fig. 4 and Figs. S2 and S3. In the 10% case, four models produce an overabundance of C to O compared to those of GS 3073. The 2000, 5000 and 7000 M_{\odot} stars have C/O ratios that are closest to the observed values, -0.45, -0.44 and -0.14, respectively at dilution factors of 5 - 15 at 2000 M_{\odot} but only at a dilution factor of 1 for 5000 and 7000 M_{\odot} . For the 50% case, three models produce an overabundance of C/O with respect to GS 3073. The 7000 M_{\odot} model most closely matches GS 3073 with a C/O ratio of -0.30 for dilution factors of 1 - 8. For the loss of all mass above the CO core, only 2 stars produce overabundances of C/O, with the 7000 M_{\odot} model again most closely matching GS 3073 with a value of -0.28 over dilution factors of 1 - 8.

Ne/O ratios

Ne/O ratios for all 10 stars are shown in the bottom right panels of Fig. 4 and Figs. S2 and S3. For 10% mass loss the 10,000 M_{\odot} star is the best match to GS 3073, with Ne/O = -0.71 at a dilution factor of ~ 20 . Only one model here produces an overabundance of Ne/O relative to GS 3073. For 50% mass loss the 9000 M_{\odot} model is the best match, with Ne/O = -0.77 at a dilution factor of ~ 20 . Two of the 10 models produce an overabundance of Ne/O. Finally, for the CO core case two stars match GS 3073, with the 2000 M_{\odot} model coming closest with Ne/O = -0.77 at a dilution factor of ~ 20 . Four models here produce an overabundance of Ne/O.

Discussion and conclusion: As shown in Fig. S4, N/O ratios for GS 3073 cannot be explained by Pop III stars above or below this mass range. 900 and 950 M_{\odot} stars evolved until the end of core O burning do not produce N/O ratios greater than -0.16, regardless of mass loss. Likewise, 15,000 M_{\odot} and 21,000 M_{\odot} stars evolved to the end of core C and He burning, respectively, produce an N/O of at most 0.19, still well below the observed 0.46. The 21,000 M_{\odot} model also has a much lower O/H + 12 ratio of 3 - 6, effectively ruling it out as a candidate. These stars strongly suggest the presence of an upper and lower limit in mass beyond which the GS 3073 N/O ratio cannot be produced.

Furthermore, as shown in Fig. S5 and discussed in the Supplementary Data, no other populations such as Wolf-Rayet stars or rapidly rotating Pop III stars can produce these abundances either. General relativistic supernovae (GR SNe; 35) of 20,000 - 30,000 M_{\odot} solar metallicity stars can produce N/O ratios greater than those in GS 3073 but not the C/O or Ne/O ratios. Also, these stars are thought to form in collisions between protogalaxies at $z \sim 8 - 10$ that are already at solar metallicity (36, 37), well above those measured for GS 3073, 0.2 - 0.3 Z_{\odot} (38). Previous studies also show that GR SNe blow most of the gas from their host galaxies, greatly delaying subsequent star formation (39-43), so it is not clear if GS 3073 could have reached its stellar mass, $10^{9.5} M_{\odot}$, at $z = 5.55$ if a GR SN had occurred early in its history.

The stars that exhibit N/O ratios greater than those in GS 3073 can still be the origin of its N/O excess. Over time, metals from these stars (the first to form in the galaxy) lead to subsequent star formation on much smaller mass scales because of efficient cooling. Previous studies (44, 45) have shown that these later generations primarily pollute the galaxy with O, not N, so N/O ratios in the galaxy fall over time. Consequently, almost any Pop III star in the 1000 - 10,000 M_{\odot} range could have produced the N/O overabundance in GS 3073 when dilution by O by later generations of stars

is considered. This scenario also explains the GS 3073 C/O ratios, which are higher than those of about half of our stars over all three mass losses. Carbon production by later generations of stars can also raise our C/O ratios to the observed values. Ours are also the only known stars that can produce the Ne/O ratio in GS 3073. While GR supernovae of metal-enriched SMSs can explain the smaller N excess in GN-z11 (10), they cannot account for Ne abundances. Not only do several of our stars match Ne/O ratios for GS 3073, some produce an overabundance of Ne that would be diluted down to the observed values by later populations of stars.

The unprecedented supersolar N/O ratio and C/O and Ne/O ratios in GS 3073 are the first conclusive evidence in the fossil abundance record of the existence of supermassive Pop III stars at the end of the cosmic Dark Ages. GS 3073 is an excellent example of these abundances because its lower redshift permits more precise measurements, without the uncertainties with GN-z11 and CEERS 1019 at higher redshifts. The N/O overabundances of some of our stars also predict that galaxies with even higher N excesses could exist at high redshifts if they are at earlier stages of star formation. These objects could be found in future surveys by the James Webb Space Telescope and the next generation of ground-based observatories in the decade to come.

References and Notes

1. D. J. Eisenstein *et al.*, Overview of the JWST Advanced Deep Extragalactic Survey (JADES). arXiv:2306.02465 (2023).
2. M. J. Rieke, *et al.*, JADES Initial Data Release for the Hubble Ultra Deep Field: Revealing the Faint Infrared Sky with Deep JWST NIRCам Imaging. *Astrophys. J. Suppl.* 269, 16 (2023).
3. S. L. Finkelstein *et al.*, The Complete CEERS Early Universe Galaxy Sample: A Surprisingly Slow Evolution of the Space Density of Bright Galaxies at $z \sim 8.5\text{--}14.5$. *Astrophys. J.* 969, L2 (2024).
4. D. D. Kocevski *et al.*, Hidden Little Monsters: Spectroscopic Identification of Low-mass, Broad-line AGNs at $z > 5$ with CEERS. *Astrophys. J.* 954, L4 (2023).
5. R. Bezanson *et al.*, The JWST UNCOVER Treasury survey: Ultradeep NIRSpec and NIRCам Observations before the Epoch of Reionization. arXiv:2212.04026 (2022).
6. J. R. Weaver *et al.*, The UNCOVER Survey: A First-look HST + JWST Catalog of 60,000 Galaxies near A2744 and beyond. *Astrophys. J. Suppl.* 270, 7 (2024).
7. C. Kobayashi, A. Ferrara, Rapid Chemical Enrichment by Intermittent Star Formation in GN-z11. *Astrophys. J.* 962, L6 (2024).
8. S. Tsiatsiou *et al.*, Rapidly rotating Population III stellar models as a source of primary nitrogen. arXiv:2404.16512 (2024).
9. D. Nandal, Y. Sibony, S. Tsiatsiou, Fast-rotating massive Population III stars as possible sources of extreme N enrichment in high-redshift galaxies. arXiv:2405.11235 (2024).
10. C. Nagele, H. Umeda, Multiple Channels for Nitrogen Pollution by Metal-enriched Supermassive Stars and Implications for GN-z11. *Astrophys. J.* 949, L16 (2023).
11. A. J. Cameron, H. Katz, M. P. Rey, A. Saxena, Nitrogen enhancements 440 Myr after the big bang: supersolar N/O, a tidal disruption event, or a dense stellar cluster in GN-z11? *Mon. Not. Royal Astron. Soc.* 523, 3516–3525 (2023).
12. Marques-Chaves, R. *et al.*, Extreme N-emitters at high redshift: Possible signatures of supermassive stars and globular cluster or black hole formation in action. *Astro. Astrophys.* 681, A30 (2024).
13. A. J. Bunker *et al.*, JADES NIRSpec Spectroscopy of GN-z11: Lyman- α emission and possible enhanced nitrogen abundance in a $z = 10.60$ luminous galaxy. *Astro. Astrophys.* 677, A88 (2023).

14. P. Senchyna *et al.*, GN-z11 in Context: Possible Signatures of Globular Cluster Precursors at Redshift 10. *Astrophys. J.* 966, 92 (2024).
15. R. L. Larson *et al.*, A CEERS Discovery of an Accreting Supermassive Black Hole 570 Myr after the Big Bang: Identifying a Progenitor of Massive $z > 6$ Quasars. *Astrophys. J.* 953, L29 (2023).
16. X. Ji *et al.*, GA-NIFS: An extremely nitrogen-loud and chemically stratified galaxy at $z \sim 5.55$. arXiv:2404.04148 (2024).
17. T. Hosokawa, H. W. Yorke, K. Inayoshi, K. Omukai, K., N. Yoshida, Formation of Primordial Supermassive Stars by Rapid Mass Accretion. *Astrophys. J.* 778, 178 (2013).
18. T. E. Woods, A. Heger, D. J. Whalen, L. Haemmerle, R. S. Klessen, On the Maximum Mass of Accreting Primordial Supermassive Stars. *Astrophys. J.* 842, L6 (2017).
19. L. Haemmerle, T. E. Woods, R. S. Klessen, Heger, A., D. J. Whalen, The evolution of supermassive Population III stars. *Mon. Not. Royal Astron. Soc.* 474, 2757–2773 (2018).
20. D. Nandal *et al.*, Explaining the high nitrogen abundances observed in high- z galaxies via Population III stars of a few thousand solar masses. *Astro. Astrophys.* 683, A156 (2024).
21. N. P. Herrington, D. J. Whalen, T. E. Woods, Modelling supermassive primordial stars with MESA. *Mon. Not. Royal Astron. Soc.* 521, 463–473 (2023).
22. D. Nandal, D. *et al.*, Critical accretion rates for rapidly growing massive Population III stars. *Astro. Astrophys.* 677, A155 (2023).
23. M. A. Latif, S. Bovino, T. Grassi, D. R. G. Schleicher, M. Spaans, How realistic UV spectra and X-rays suppress the abundance of direct collapse black holes. *Mon. Not. Royal Astron. Soc.* 446, 3163–3177 (2015).
24. A. T. P. Schauer, D. J. Whalen, S. C. O. Glover, R. S. Klessen, Lyman-Werner UV escape fractions from primordial haloes. *Mon. Not. Royal Astron. Soc.* 454, 2441–2450 (2015).
25. L. R. Prole *et al.*, Heavy black hole seed formation in high- z atomic cooling halos. *Astro. Astrophys.* 685, A31 (2024).
26. J. H. Wise, M. J. Turk, T. Abel, Resolving the Formation of Protogalaxies. II. Central Gravitational Collapse. *Astrophys. J.* 682, 745–757 (2008).
27. J. A. Regan, M. G. Haehnelt, Pathways to massive black holes and compact star clusters in pre-galactic dark matter haloes with virial temperatures > 10000 K. *Mon. Not. Royal Astron. Soc.* 396, 343–353 (2009).
28. M. A. Latif, D. R. G. Schleicher, W. Schmidt, J. C. Niemeyer, The characteristic black hole mass resulting from direct collapse in the early Universe. *Mon. Not. Royal Astron. Soc.* 436, 2989–2996 (2013).
29. S. J. Patrick, D. J. Whalen, M. A. Latif, J. S. Elford, The collapse of atomically cooled primordial haloes - I. High Lyman-Werner backgrounds. *Mon. Not. Royal Astron. Soc.* 522, 3795–3808 (2023).
30. M. A. Latif, S. Khochfar, D. Schleicher, D. J. Whalen, Radiation hydrodynamical simulations of the birth of intermediate-mass black holes in the first galaxies. *Mon. Not. Royal Astron. Soc.* 508, 1756–1767 (2021).
31. D. J. Whalen, C. L. Fryer, The Formation of Supermassive Black Holes from Low-mass PopIII Seeds. *Astrophys. J.* 756, L19 (2012).
32. J. Smidt, D. J. Whalen, J. L. Johnson, M. Surace, H. Li, Radiation Hydrodynamical Simulations of the First Quasars. *Astrophys. J.* 865, 126 (2018).
33. M. A. Latif, D. J. Whalen, S. Khochfar, N. P. Herrington, T. E. Woods, Turbulent cold flows gave birth to the first quasars. *Nature* 607, 48–51 (2022).
34. P. Eggenberger *et al.*, The Geneva stellar evolution code. *Ap&SS* 316, 43–54 (2008).

35. C. Nagele, H. Umeda, K. Takahashi, T. Yoshida, K. Sumiyoshi, Stability analysis of supermassive primordial stars: a new mass range for general relativistic instability supernovae. *Mon. Not. Royal Astron. Soc.* 517, 1584–1600 (2022).
36. L. Mayer, S. Kazantzidis, A. Escala, S. Callegari, Direct formation of supermassive black holes via multi-scale gas inflows in galaxy mergers. *Nature* 466, 1082–1084 (2010).
37. L. Mayer, L., S. Bonoli, The route to massive black hole formation via merger-driven direct collapse: a review. *Reports on Progress in Physics* 82, 016901 (2019).
38. Ubler, H. *et al.*, GA-NIFS: A massive black hole in a low-metallicity AGN at $z \sim 5.55$ revealed by JWST/NIRSpec IFS. *Astro. Astrophys.* 677, A145 (2023).
39. D. J. Whalen *et al.*, Supermassive Population III Supernovae and the Birth of the First Quasars. *Astrophys. J.* 778, 17 (2013).
40. D. J. Whalen *et al.*, The Supernova that Destroyed a Protogalaxy: Prompt Chemical Enrichment and Supermassive Black Hole Growth. *Astrophys. J.* 774, 64 (2013).
41. D. J. Whalen *et al.* The Biggest Explosions in the Universe. II. *Astrophys. J.* 777, 99 (2013).
42. J. L. Johnson *et al.* The Biggest Explosions in the Universe. *Astrophys. J.* 775, 107 (2013).
43. K.-J. Chen *et al.*, The General Relativistic Instability Supernova of a Supermassive Population III Star. *Astrophys. J.* 790, 162 (2014).
44. S. Ekstrom *et al.*, Grids of stellar models with rotation. I. Models from 0.8 to 120 M_{\odot} at solar metallicity ($Z = 0.014$). *Astro. Astrophys.* 537, A146 (2012).
45. L. J. Murphy *et al.*, Grids of stellar models with rotation - V. Models from 1.7 to 120 M_{\odot} at zero metallicity. *Mon. Not. Royal Astron. Soc.* 501, 2745–2763 (2021).
46. L. Henyey, M. S. Vardya, P. Bodenheimer, Studies in Stellar Evolution. III. The Calculation of Model Envelopes. *Astrophys. J.* 142, 841 (1965).
47. F. X. Timmes, F. D. Swesty, The Accuracy, Consistency, and Speed of an Electron-Positron Equation of State Based on Table Interpolation of the Helmholtz Free Energy. *Astrophys. J. Suppl.* 126, 501–516 (2000).
48. C. A. Iglesias, F. J. Rogers, Updated Opal Opacities. *Astrophys. J.* 464, 943 (1996).
49. F. J. Rogers, F. J. Swenson, C. A. Iglesias, OPAL Equation-of-State Tables for Astrophysical Applications. *Astrophys. J.* 456, 902 (1996).
50. F. J. Rogers, A. Nayfonov, Updated and Expanded OPAL Equation-of-State Tables: Implications for Helioseismology. *Astrophys. J.* 576, 1064–1074 (2002).
51. D. Nandal, E. Farrell, G. Buldgen, G. Meynet, S. Ekstrom, The evolution and impact of $\sim 3000 M_{\odot}$ stars in the early Universe. *Astro. Astrophys.* 685, A159 (2024).
52. L. Haemmerlé, P. Eggenberger, G. Meynet, A. Maeder, C. Charbonnel, Star formation with disc accretion and rotation. I. Stars between 2 and 22 M_{\odot} at solar metallicity. *Astro. Astrophys.* 557, A112 (2013).
53. L. Haemmerlé, P. Eggenberger, G. Meynet, A. Maeder, A., C. Charbonnel, Massive star formation by accretion. I. Disc accretion. *Astro. Astrophys.* 585, A65 (2016).
54. F. Palla, S. W. Stahler, The Evolution of Intermediate-Mass Protostars. II. Influence of the Accretion Flow. *Astrophys. J.* 392, 667 (1992).
55. T. Hosokawa, H. W. Yorke, K. Omukai, Evolution of Massive Protostars Via Disk Accretion. *Astrophys. J.* 721, 478–492 (2010).
56. J. S. Vink, A. de Koter, A., H. J. G. L. M. Lamers, Mass-loss predictions for O and B stars as a function of metallicity. *Astro. Astrophys.* 369, 574–588 (2001).
57. L. Haemmerlé, T. E. Woods, R. S. Klessen, A. Heger, A. D. J. Whalen, On the Rotation of Supermassive Stars. *Astrophys. J.* 853, L3 (2018).

58. G. M. Fuller, S. E. Woosley, S. E., T. A. Weaver, The evolution of radiation-dominated stars. I - Nonrotating supermassive stars. *Astrophys. J.* 307, 675–686 (1986).
59. H. Saio, D. Nandal, S. Ekstroem, G. Meynet, Linear adiabatic analysis for general relativistic instability in primordial accreting supermassive stars. arXiv:2406.18040 (2024).
60. S. W. Stahler, F. Palla, E. E. Salpeter, Primordial stellar evolution - The protostar phase. *Astrophys. J.* 302, 590–605 (1986).
61. Y. Sakurai, T. Hosokawa, N. Yoshida, H. W. Yorke, Formation of primordial supermassive stars by burst accretion. *Mon. Not. Royal Astron. Soc.* 452, 755–764 (2015).
62. S. E. Woosley, S. Blinnikov, A. Heger, Pulsational pair instability as an explanation for the most luminous supernovae. *Nature* 450, 390–392 (2007).
63. D. J. Whalen *et al.*, Finding the First Cosmic Explosions. III. Pulsational Pair-instability Supernovae. *Astrophys. J.* 781, 106 (2014).
64. K.-J. Chen, S. E. Woosley, A. Heger, A. Almgren, D. J. Whalen, Two-dimensional Simulations of Pulsational Pair-instability Supernovae. *Astrophys. J.* 792, 28 (2014).
65. S. E. Woosley, Pulsational Pair-instability Supernovae. *Astrophys. J.* 836, 244 (2017).
66. S.-C. Leung, K. Nomoto, S. Blinnikov, Pulsational Pair-instability Supernovae. I. Pre-collapse Evolution and Pulsational Mass Ejection. *Astrophys. J.* 887, 72 (2019).
67. K.-J. Chen, D. J. Whalen, S. E. Woosley, W. Zhang, Multidimensional Radiation Hydrodynamics Simulations of Pulsational Pair-instability Supernovae. *Astrophys. J.* 955, 39 (2023).
68. G. Rakavy, G. Shaviv, Instabilities in Highly Evolved Stellar Models. *Astrophys. J.* 148, 803 (1967).
69. Z. Barkat, G. Rakavy, N. Sack, Dynamics of Supernova Explosion Resulting from Pair Formation. *Physical Review Letters* 18, 379–381 (1967).
70. D. J. Whalen *et al.*, Finding the First Cosmic Explosions. I. Pair-instability Supernovae. *Astrophys. J.* 777, 110 (2013).
71. D. J. Whalen *et al.*, Pair-instability Supernovae in the Local Universe. *Astrophys. J.* 797, 9 (2014).
72. Q.-F. Xing *et al.*, A metal-poor star with abundances from a pair-instability supernova. *Nature* 618, 712–715 (2023).
73. T. A. Weaver, G. B. Zimmerman, S. E. Woosley, Presupernova evolution of massive stars. *Astrophys. J.* 225, 1021–1029 (1978).
74. S. E. Woosley, A. Heger, T. A. Weaver, The evolution and explosion of massive stars. *Reviews of Modern Physics* 74, 1015–1071 (2002).
75. Q. Zhu *et al.*, The Formation of the First Quasars. I. The Black Hole Seeds, Accretion and Feedback Models. *Mon. Not. Royal Astron. Soc.* 514, 5583–5606 (2022).
76. C. Nagele, H. Umeda, K. Takahashi, K. Maeda, Pulsations of primordial supermassive stars induced by a general relativistic instability; visible to JWST at $z > 12$. *Mon. Not. Royal Astron. Soc.* 520, L72–L77 (2023).
77. A. Maeder, G. Meynet, Stellar evolution with rotation. VI. The Eddington and Omega - limits, the rotational mass loss for OB and LBV stars. *Astro. Astrophys.* 361, 159–166 (2000).
78. D. Schaerer, R. Pello, Towards observations of Population III galaxies. In K. van der Hucht, A. Herrero, C. Esteban (eds.) *A Massive Star Odyssey: From Main Sequence to Supernova*, vol. 212, 747 (2003).
79. C. Chiappini *et al.*, A new imprint of fast rotators: low $^{12}\text{C}/^{13}\text{C}$ ratios in extremely metal-poor halo stars. *Astro. Astrophys.* 479, L9–L12 (2008).

80. J. H. Wise, T. Abel, Suppression of H₂ Cooling in the Ultraviolet Background. *Astrophys. J.* 671, 1559–1567 (2007).
81. B. W. O’Shea, M. L. Norman, Population III Star Formation in a Λ CDM Universe. II. Effects of a Photodissociating Background. *Astrophys. J.* 673, 14–33 (2008).
82. A. Heger, S. E. Woosley, The Nucleosynthetic Signature of Population III. *Astrophys. J.* 567, 532–543 (2002).
83. A. Heger, S. E. Woosley, Nucleosynthesis and Evolution of Massive Metal-Free Stars. *Astrophys. J.* 724, 341–373 (2010).
84. J. A. Regan, E. Visbal, J. H. Wise, Z. Haiman, P. H. Johansson, G. L. Bryan, Rapid formation of massive black holes in close proximity to embryonic protogalaxies. *Nat. Astron.* 1, 75, (2017).
85. B. Liu, V. Bromm, When did Population III star formation end? *Mon. Not. Royal Astron. Soc.* 497, 2839–2854 (2020).
86. A. Venditti, *et al.*, A needle in a haystack? Catching Population III stars in the epoch of reionization: I. Population III star-forming environments. *Mon. Not. Royal Astron. Soc.* 522, 3809–3830 (2023).

Acknowledgments:

Funding

VITA Fellowship (DN)

ERC Grant 833925 (Project STAREX) (DN)

United Arab Emirates University UPAR Grant 31S390 (MAL)

United Arab Emirates University UPAR Grant 12S111 (MAL)

Australian Research Council Grant DP240101786 (AH)

Australian Research Council Grant DP240103174 (AH)

Author contributions

Conceptualization: DN, DJW

Methodology: DN, MAL, AH

Investigation: DN, DJW, MAL, AH

Visualization: DN, MAL

Supervision: DN, DJW

Writing – original draft: DN, DJW

Writing – review & editing: DJW

Competing interests: Authors declare that they have no competing interests.

Data and materials availability: GENEC and its parameter files and outputs are available upon reasonable request from DN.

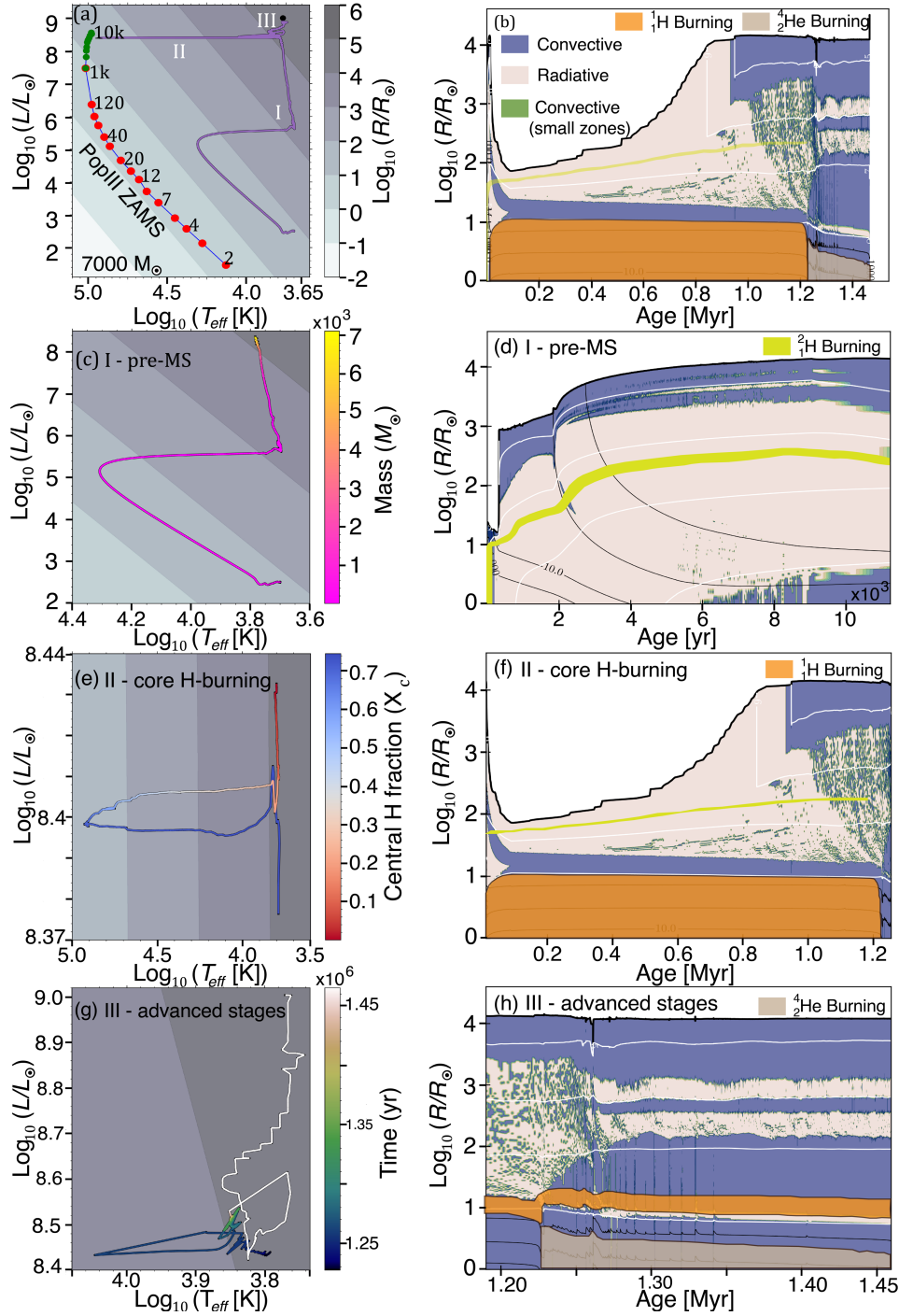


Fig. 1. HR (left) and Kippenhahn diagrams (right) for the $7000 M_{\odot}$ star. The entire evolution of the star is shown in (a) and (b), its pre-MS evolution is shown in (c) and (d), its core H burning phase is in (e) and (f), and core He burning to the end of Si burning are in (g) and (h). The black and white lines in the Kippenhahn diagrams are isomass and isothermal lines, respectively, and the red and green dots along the track on the lower left in (a) are the zero-age main sequence (ZAMS) positions of 2 - 120 M_{\odot} and 1000 - 10,000 M_{\odot} Pop III stars for comparison.

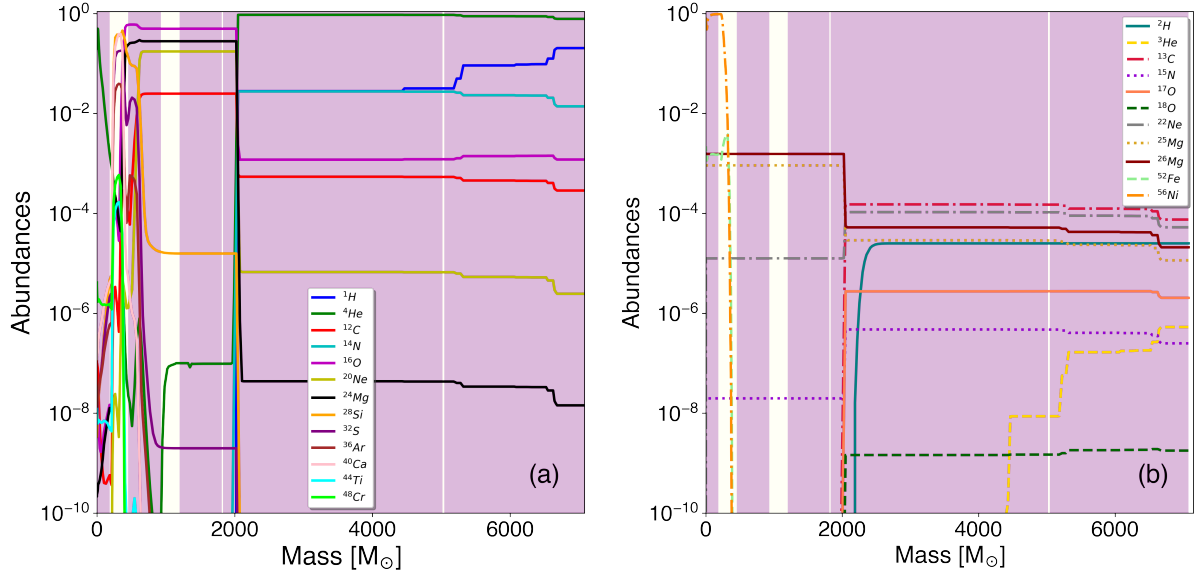


Fig. 2. Abundance profiles of the 7000 M_{\odot} star at the end of Si burning. Purple and white regions are convective and radiative zones, respectively.

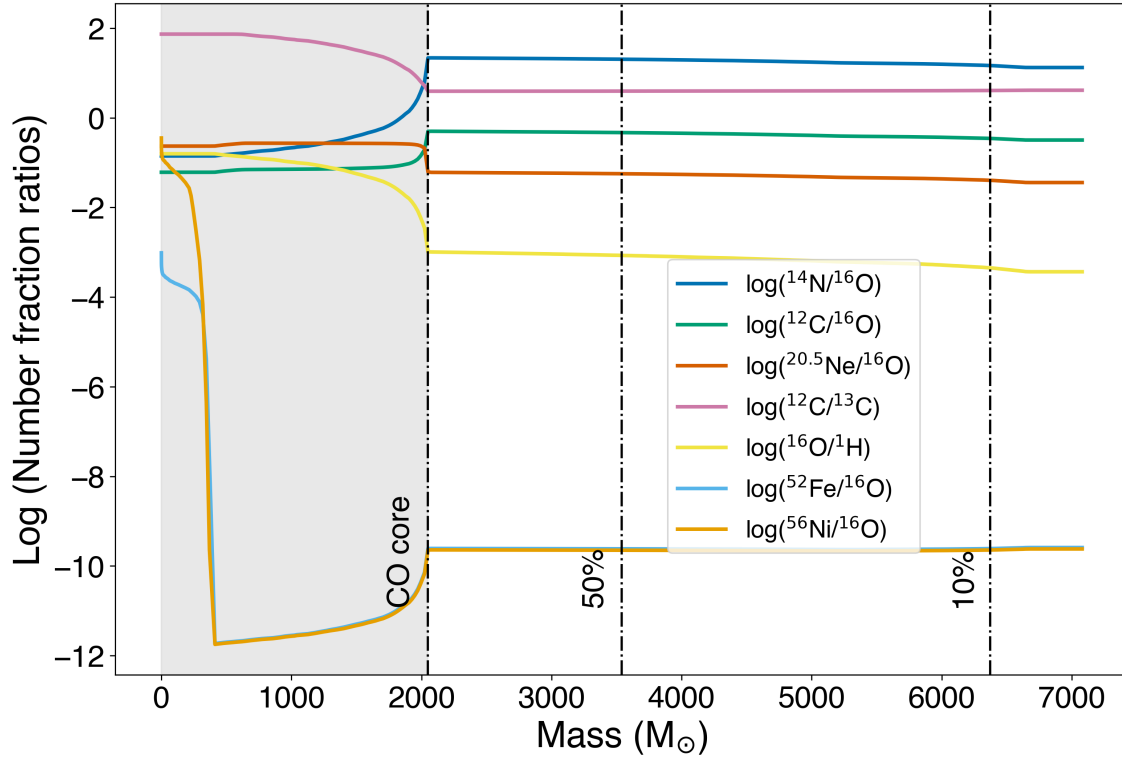


Fig. 3. Element number ratios in the 7000 M_{\odot} star at the end of Si burning. The masses used to calculate the ratios at a mass coordinate are cumulative, from the stellar atmosphere on the right to the depth corresponding to the given mass loss on the left.

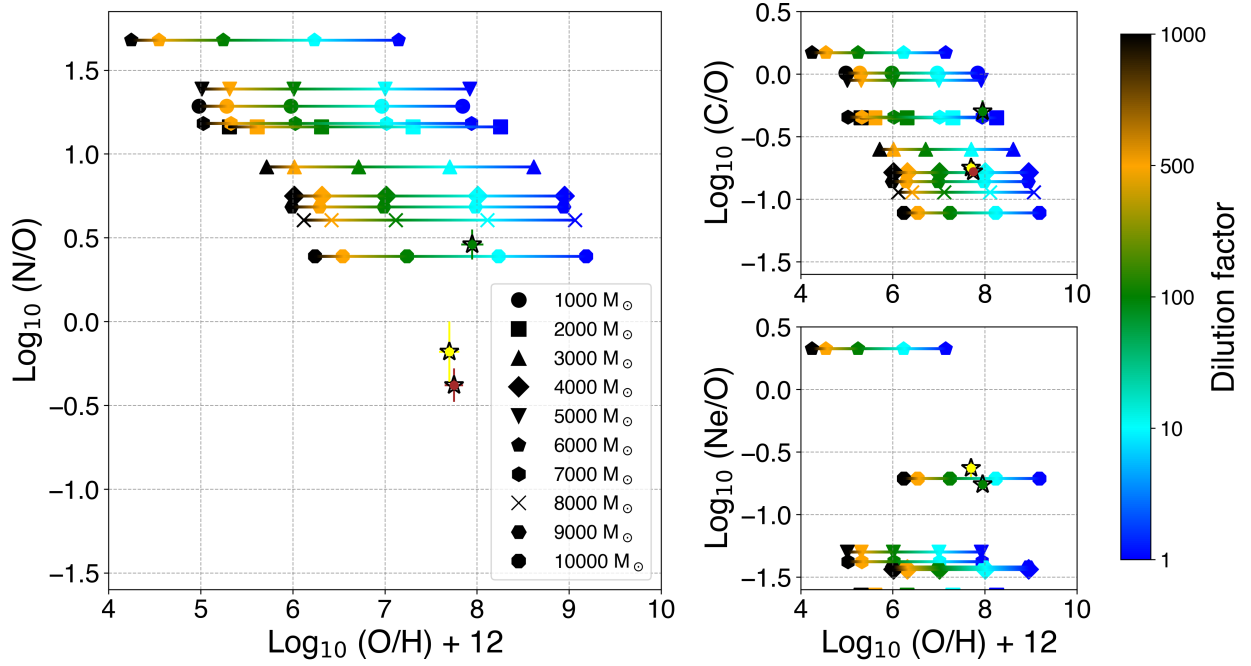


Fig. 4. N/O, C/O and Ne/O number ratios for 1000 - 10,000 M_{\odot} Pop III stars, assuming 10% mass loss. The green, yellow, and brown stars indicate corresponding ratios for GS 3073

(16), CEERS 1019 and GN-z11, respectively. The dilution factor is the mass of the gas contaminated by outflows from the star divided by the mass of the outflow.



Supplementary Materials for

1000 - 10,000 M_{\odot} primordial stars created the nitrogen excess in the galaxy GS 3073 at $z = 5.55$

Devesh Nandal^{1*}, Daniel J. Whalen^{2*}, Muhammad A. Latif³, Alexander Heger⁴
Corresponding authors: deveshnandal@yahoo.com, dwhalen1999@gmail.com

The PDF file includes:

Supplementary Text
Figs. S1 to S11
Table S1
References 46-86

Supplementary Text

GENEC is a 1D Lagrangian stellar evolution code that uses the Henyey method (46) to solve the equations of stellar structure. Energy generation and nucleosynthesis is calculated with a 38-isotope reaction network that includes hot CNO cycles and we use the Helmholtz equation of state (47), which includes contributions from degenerate and non-degenerate relativistic and non-relativistic electrons, electron-positron pair production, and radiation. Internal opacities are derived from the OPAL tables (48-50) and convection is approximated by mixing-length theory.

We initialize the stars as $2 M_{\odot}$ hydrostatic $n \sim 3/2$ polytropes with uniform entropy profiles. They have a homogeneous chemical composition (44,45,51) with $X = 0.7516$, $Y = 0.2484$, and $Z = 0$ and a deuterium mass fraction (19,22) $X_2 = 5 \times 10^{-5}$. They are initially evolved with accretion rates above $2 \times 10^{-2} M_{\odot} \text{ yr}^{-1}$, the critical rate above which the protostars grow as cool, red supergiants (21,22). These rates are later increased as the stars approach the Hayashi limit for the first time to ensure that they reach their target masses by the end of the pre-main sequence or at the onset of core hydrogen burning, after which accretion is terminated. We assume cold accretion (17), in which the entropy of the accreting material is matched to that of the surface of the star (19) and is assumed to be radiated away, as in geometrically thin, cold disks (52,53). Any excess entropy in the infalling matter is radiated away before reaching the surface of the star (54,55).

As Pop III stars form from pristine gas, we exclude line-driven winds from our models (56). We evolve all ten stars to the end of core oxygen burning and a few to the end of silicon burning. The stars are partitioned into up to 420 zones in mass and are adaptively rezoned over their evolution. The stars were also evolved with adaptive time steps, and a moderate convective overshoot of 0.100 in the pre-main sequence and core hydrogen burning stages but not at later stages. Rotation is not included in our models (57). We apply the first-order post-Newtonian Tolman-Oppenheimer-Volkoff (TOV) correction to the equation of hydrostatic equilibrium throughout the evolution of the stars to accommodate GR effects by modifying Newton's gravitational constant, G (18,19,58):

$$G_{rel} = \left(1 + \frac{P}{\rho c^2} + \frac{2GM_r}{rc^2} + \frac{4\pi Pr^3}{M_r c^2} \right)$$

where P is the pressure, ρ the mass density, c the speed of light and M_r is the mass enclosed by radius r . We have since confirmed by linear stability analysis that none of the stars in our study encounter the GR instability at any point in their evolution (59).

7000 M_{\odot} Pop III star evolution

Here, we review the evolution of a 7000 M_{\odot} star.

Protostar growth

The seed is initialized with accretion rates of $0.025 - 3 M_{\odot} \text{ yr}^{-1}$, so it evolves as a red supergiant protostar (21,22). As it grows in mass its central temperatures reach 10^6 K and trigger deuterium burning at $3.2 M_{\odot}$ as shown by the yellow band in panel (d) of Fig. 1. Deuterium fusion does not

produce enough energy to halt internal contraction so central temperatures continue to rise. The luminosity and surface temperature of the protostar increase as it grows in mass so its HR track migrates up and to the left in panel (c) of Fig. 1. Rising core temperatures then drive an outward luminosity wave (60,61) lasting for ~ 100 yr that causes the protostar to expand and cool at $18 M_{\odot}$, and the HR track veers back to the right and then evolves along the nearly vertical Hayashi limit. As shown in panel (d), the protostar has a large convective envelope over a radiative zone for most of its evolution until a central convective zone appears as the star approaches core H burning.

Central H burning

After accretion is halted at 12,000 yr when the protostar reaches $7000 M_{\odot}$, its structure settles on a Kelvin-Helmholtz (KH) timescale $\tau_{KH} = GM^2 / 2RL \sim 80,000$ yr and it evolves to the left in the HR diagram in panel (e) as it becomes hotter and brighter. Rising core temperatures due to KH contraction activate central H burning at $\log_{10}(T_{\text{eff}} [\text{K}]) = 4.3$ and then the triple- α chain. Carbon from the triple α - α activates CNO burning, which finally halts contraction and the star settles onto the main sequence. The model reaches the leftmost point in the HR diagram in (e) at 95,000 yr but then migrates back to the right as energy released by central H burning expands and cools the star. As shown in panel (f), by 0.1 Myr the star has a structure similar to those of 9 - $120 M_{\odot}$ stars, with a convective core that recedes in mass as central H burning proceeds and a radiative envelope that grows in radius over time. Changes in adiabatic gradients (∇_{rad} and ∇_{ad}) promote the formation of a large number of small convective zones in the radiative region after 0.4 Myr. A large convective zone also forms in the outer envelope when the star reaches radii $\log_{10}(R/R_{\odot}) > 4$. At 1.22 Myr the model has depleted all of its core hydrogen and exits the main sequence.

Post-main sequence evolution

Central helium burning begins at 1.2 Myr at $\log_{10}(T_{\text{eff}} [\text{K}]) = 3.85$ and $\log_{10}(L/L_{\odot}) = 8.50$ in panel (g) of Fig. 1. At 1.227 Myr the convective core has a helium-burning center with an outer convective boundary as shown in panel (h). Above the convective core lies a thin radiative zone and the convective H burning shell. Several small convective regions appear in the radiative layer over the course of central He burning. Above the H burning shell there are also large convective zones, radiative zones with convective cells, and finally very large convective envelopes. The structure of the star is thus primarily convective at late times.

Carbon burning begins at 1.35 Myr, before the end of central He burning at 1.465 Myr because high central temperatures allow C to fuse as soon as it is produced by He. Ne burning, mostly ^{20}Ne , then begins but only lasts for 10 hours and produces ^{16}O via photodisintegration at temperatures of 12×10^9 K. Alpha particles from photodisintegration react with ^{20}Ne to form ^{24}Mg . Because of its short duration, Ne burning begins and ends at the same point in the HR diagram, at $\log_{10}(T_{\text{eff}} [\text{K}]) = 3.84$ and $\log_{10}(L/L_{\odot}) = 8.51$ in panel (g). Core O burning then begins and finishes in 41 minutes, with subsequent Si burning that lasts for just a few minutes after which the run is ended at 1.46 Myr.

Collapse

As shown in Fig. S6, all ten stars enter the pair instability (PI) regime at the end of their lives. In less massive Pop III stars the PI can lead to violent pulsational mass loss (62-67) or an explosion that completely unbinds the star (68-72). However, even if the PI triggers explosive thermonuclear burning in O and Si in these stars it is unlikely that the energy released would reverse their collapse because of their large masses. To test this point we evolved the 8000 M_{\odot} star from the end of Ne burning to collapse in the Kepler stellar evolution code (73,74) because it can transition to hydrodynamics to follow explosions and collapse. We find that even though the star encounters the PI, photodisintegrations also crack heavy elements into alpha particles and then alphas into nucleons in the core. The corresponding loss of thermal pressure triggers rapid collapse of the core, and the central 1200 M_{\odot} of the star reaches infall velocities of 10% of the speed of light by the end of the simulation, as shown in Fig. S7. The kinetic energy of this mass is several MeV/nucleon, more than nuclear burning can yield. The other stars would likely have similar fates. Some elements may be explosively synthesized during collapse, but they would almost certainly be swallowed by the BH because there is so much mass in the outer layers of the star.

Because these stars collapse, massive black holes would be a general feature of high-redshift galaxies with large N/O ratios, and a supermassive star may well have been the origin of the Type-1 AGN in GS 3073, which has $\log_{10}(M_{\text{BH}}) = 8.2 \pm 0.4$ at $z = 5.55$. As shown in Fig. S8, even a 1000 M_{\odot} star that has lost 50% of its mass can reach $10^{8.2} M_{\odot}$ by this redshift at sub-Eddington accretion rates if it is born at $z \gtrsim 15$. Such accretion rates are less than those required to form quasars (32,33,75) at $z > 6$. Consequently, the discovery of massive BHs in high-redshift galaxies with large N/O ratios in future surveys would reinforce our enrichment scenario.

Mass loss

Although 1000 - 10,000 M_{\odot} Pop III stars collapse to black holes without exploding, they can still chemically enrich their host galaxies. Mass loss in these stars is not well understood but they are likely prone to pulsations that would eject a fraction of their envelopes at some point in their evolution, especially late in their lives. Prior to the depletion of central H the stars are relatively compact, with $\log_{10}(R/R_{\odot}) = 1.0 - 1.5$, so it would be more difficult for pulsations to eject mass from these depths in their potential wells. Later, during central He burning, the star can swell to much larger radii ($\log_{10}(R/R_{\odot}) = 4.0 - 4.5$) and lower surface gravities that are more conducive to expulsion. At this stage the stars also have small β ($= P_{\text{gas}}/(P_{\text{gas}} + P_{\text{rad}})$) and are therefore largely dominated by radiation pressure, which can also drive mass loss.

Although all ten stars encounter the PI late in nuclear burning, it does not result in changes in their structures that would indicate pulsations or expulsions of mass in our models. This is true even of the 7000 M_{\odot} star, the inner 13% of which in mass is enveloped by the PI regime. While we include post-Newtonian corrections to gravity due to general relativistic effects, they never trigger pulsations that could result in mass loss or collapse (76). This is consistent with previous studies that indicate that Pop III stars are not prone to the GR instability below a few $10^4 M_{\odot}$ (21,35).

Rotation

Rotation is expected to enhance nitrogen production in massive stars. However, it has never been included in studies of 1000 - 10,000 M_{\odot} stars and is challenging to model in Pop III stars above

100 M_{\odot} because of the Ω - Γ limit, the maximum rotation a star can have without being unbound by radiation and centrifugal forces (77). Although studies suggest that supermassive stars cannot tolerate much rotation because gravity cannot hold the star together against their extreme outward radiation pressures and centrifugal effects (at most a few percent of Keplerian; 57), they are all expected to have some. We consider the effect of rotation on nitrogen yields from the 5000 M_{\odot} star evolved up to the onset of core helium burning ($Y_c = 0.9$) with an initial rotation rate of $0.1v/v_{\text{crit}}$. This evolutionary stage is particularly important because the star becomes fully convective at the onset of core helium burning. N/O ratios with and without rotation are shown for the star at $Y_c = 0.9$ for the case of 10% mass loss in Fig. S9. We find that rotation results in only a marginal enhancement in N/O, indicating that chemical transport in these stars is primarily dominated by the convective zones that develop during this phase with rotation having a secondary effect.

Progenitor mass

We find no direct dependence of surface abundances on progenitor mass from 1000 - 10,000 M_{\odot} . Enrichment of the surface is primarily due to the formation of the many convective zones in the star as it transitions to a red supergiant at the onset of He burning, especially in the intermediate regions shown in panels (f) and (h) of Fig. 1. The lynchpin of this transport mechanism is the close proximity of the hydrogen burning shell to the convective core. Stars in which there is greater separation between the two exhibit less transport of carbon, which results in less production of N and less enrichment of the surface. Surface abundances are therefore less a matter of progenitor mass (since 900 and 15,000 M_{\odot} stars cannot reproduce the GS 3073 ratios) and more a function of convective mixing.

N/O ratios of other stellar populations

We show N/O ratios for a variety of stellar populations and initial mass functions (IMFs) in Fig. S5. We consider stars with masses of 9, 12, 15, 20, 25, 30, 32, 40, 60, 85, and 120 M_{\odot} evolved until the end of core helium burning at metallicities $Z = 0, 10^{-5}, 10^{-4}, 0.002, 0.006, 0.014,$ and 0.020 . We examine Salpeter, top-heavy, and flat IMFs but do not account for dilution and instead focus on the N/O ratios of stellar ejecta. As metallicity rises, mass loss due to stellar winds, particularly during core helium burning, becomes important and is included in our models. We find that no single stellar model in this mass range produces N/O ratios consistent with GS 3073 and that averaging the yields of the 11 models with Salpeter and top-heavy IMFs at each metallicity also fails to replicate the observed ratios. Even when assuming populations of 10^5 stars distributed over the same mass range the N/O ratios remain far below observed values.

Rotation is expected to enhance nitrogen production in massive stars so we also examine yields from stars with initial rotation rates $v/v_{\text{crit}} = 0.4$ over the same mass range (9 - 120 M_{\odot}) and IMFs, but they do not produce the observed N/O ratios. Increasing the initial rotation to $v/v_{\text{crit}} = 0.7$ shows better agreement with GN-z11 but still falls short of GS 3073. No combination of metallicity, population size, rotation rate, or IMF in the 9 - 120 M_{\odot} range accounts for the high N/O ratios in high redshift galaxies. Flat, Salpeter, and top-heavy IMF averages of the yields of our 1000 - 10,000 M_{\odot} stars result in N/O ratios that are consistent with observations, suggesting that nitrogen production in the early universe may be dominated by such stars rather than those below 120 M_{\odot} .

He/H and $^{12}\text{C}/^{13}\text{C}$ ratios

We show He/H ratios, a prominent observational feature of massive stars (78), for all ten stars and three mass loss cases versus $\log_{10}(\text{O}/\text{H}) + 12$ measured for GS 3073 in Fig. S10. For 10% mass loss the 5000 and 7000 M_{\odot} stars have $\log_{10}(\text{He}/\text{H})$ of -0.55 and -0.53, respectively, at a dilution factor of 1. These ratios are strongly dependent on dilution factor and all the models except 6000 M_{\odot} produce $\log_{10}(\text{He}/\text{H})$ from -0.63 to -1.00 at dilution factors of 1 - 200. For 50% mass loss the 5000 and 7000 M_{\odot} stars exhibit $\log_{10}(\text{He}/\text{H})$ of -0.46 and -0.48, respectively, at dilution factors of 1 - 2 while other stars have $\log_{10}(\text{He}/\text{H})$ from -0.65 to 1.00 at dilution factors of 1 - 250. In the case of mass loss down the CO core, the ratios for all the stars are similar to those for 50% mass loss. He/H ratios are very sensitive to contributions from subsequent populations of stars and change as the galaxy evolves over time.

$^{12}\text{C}/^{13}\text{C}$ ratios are an important signature of CNO burning in massive stars. We find ^{12}C and ^{13}C masses to be boosted by mixing between the convective He and H core and shell. For the $\log_{10}(\text{O}/\text{H}) + 12$ ratio measured for GS 3073, we find $\log_{10}(^{12}\text{C}/^{13}\text{C}) = 0.59 - 0.65$ for dilution factors of 1 - 150. 1000 M_{\odot} is an outlier, with $\log_{10}(^{12}\text{C}/^{13}\text{C}) = 0.800$. These ratios are similar for all three cases of mass loss and are consistent with those of rapidly rotating massive stars (79).

Fe/O ratios

Large Fe/O abundances have also been reported for GS 3073, albeit with large uncertainties (16). The stars in our study create enough end stage Fe to account for these ratios but it almost certainly is swallowed up by the BH during collapse. However, the moderate LW UV backgrounds that led to the formation of the supermassive Pop III star were also conducive to the formation of 140 - 260 M_{\odot} Pop III stars (80,81), which die as PI SNe that can produce up to tens of solar masses of ^{56}Ni that eventually decay to Fe (82,83). The large Fe masses in GS 3073 may therefore have come from less massive Pop III stars that form roughly at the same time as the SMS.

UV / optical observations of GS 3073 N/O ratios

Gas at lower densities in GS 3073, as traced by optical lines, has a much lower N/O = -1.1 than gas at high densities, which is traced by UV lines (16). One possibility is that the SMS formed in a satellite halo and later merged with GS 3073, in which a mature population of stars had already formed (84). Another is that the SMS formed in a pristine pocket of gas in GS 3073 in the presence of a well-established stellar population (85,86). We test this scenario by using the C, N, and O fractions in the low-density gas in GS 3073 from Figures 4 and 8 of Ji et al. 2024 to calculate the metallicity floor that was in place at the time of SMS formation. We find N, O, C and Ne mass fractions of 8.0×10^{-5} , 1.2×10^{-3} , 2.8×10^{-4} and 9.4×10^{-4} , respectively. We then mix ejecta from the SMS with the ISM for a range of dilution factors. As shown in the N/O subplot of Fig. S11, mixing by most of the SMSs produces a nearly vertical climb in N/O ratio from its floor of -1.1 to 0.46 with no change in the O/H ratio, in good agreement with Figure 4 of Ji et al. 2024. Besides showing that most of the SMSs can enrich dense gas in GS 3073 to an N/O ratio 0.46, this test also shows that they must be Pop III stars because any other stars would not keep O/H constant. Consequently, gas pocket SMS formation is one scenario that is in good agreement with Ji et al 2024. Because these observations are preliminary and the distribution of low-metallicity and high-metallicity gas in GS 3073 is not yet known, it is not yet possible to determine precisely which

enrichment scenario happened, only that massive nitrogen production by supermassive stars must have occurred.

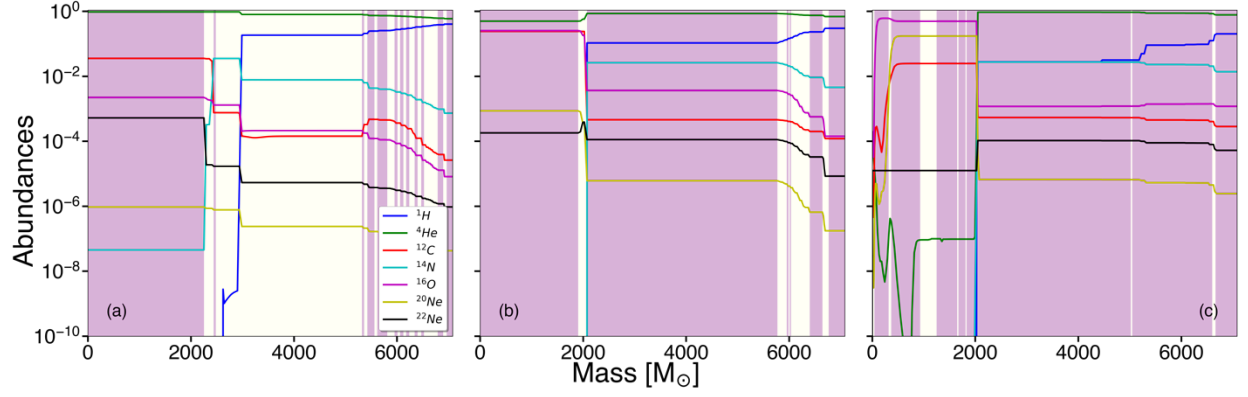


Fig. S1. Abundance profiles of the 7000 M_{\odot} star at the beginning (a), middle (b) and end (c) of core He burning.

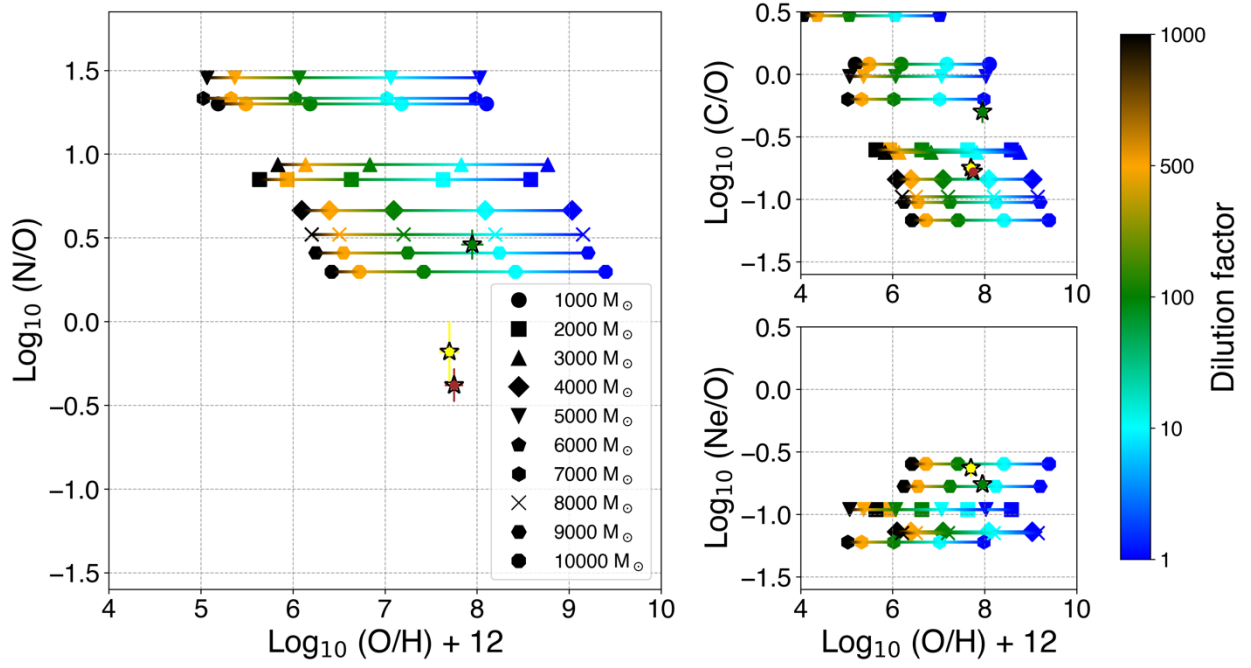


Fig. S2. N/O, C/O and Ne/O number ratios for 50% mass loss. The green, yellow, and brown stars denote corresponding ratios for GS 3073, CEERS 1019 and GN-z11, respectively.

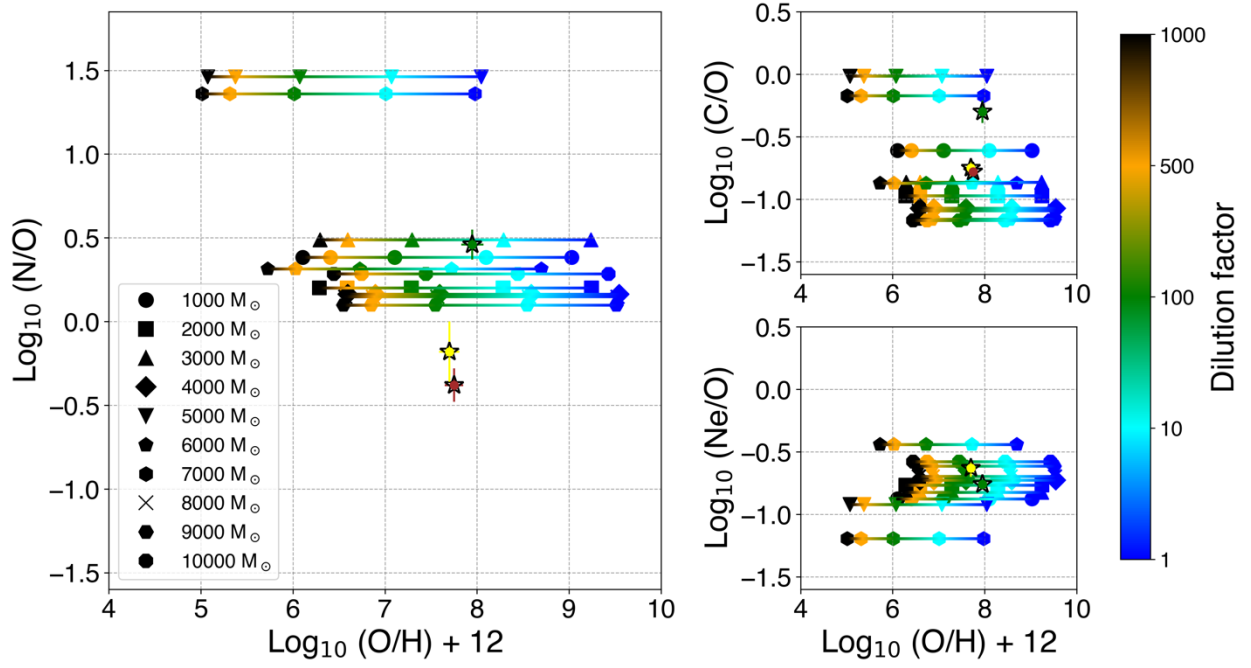


Fig. S3. N/O, C/O and Ne/O number ratios for the loss of all the mass above the CO core. Green, yellow and brown stars mark corresponding ratios for GS 3073, CEERS 1019 and GN-z11.

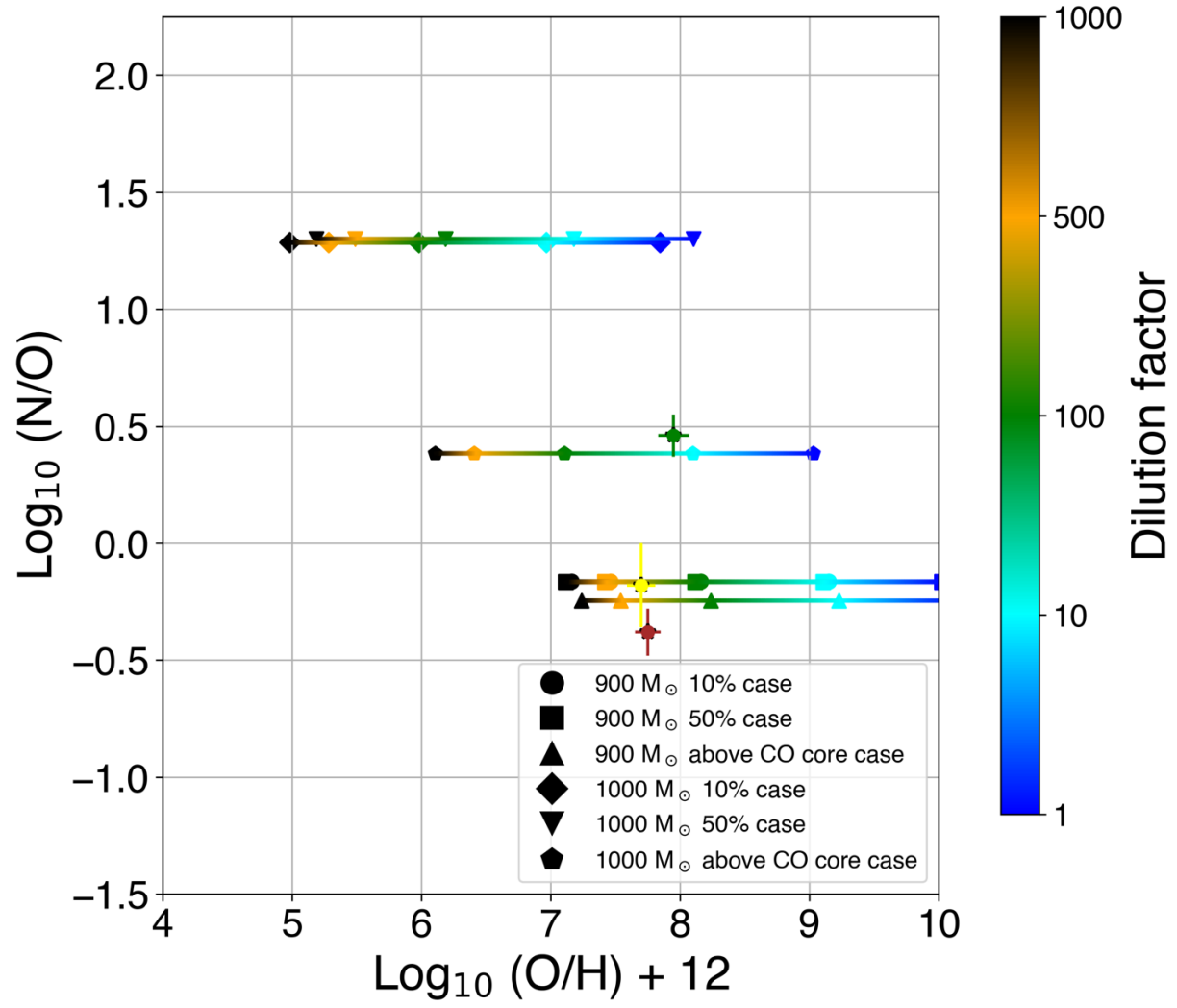


Fig. S4. N/O ratios for the 900 and 1000 M_{\odot} stars for all three mass losses.

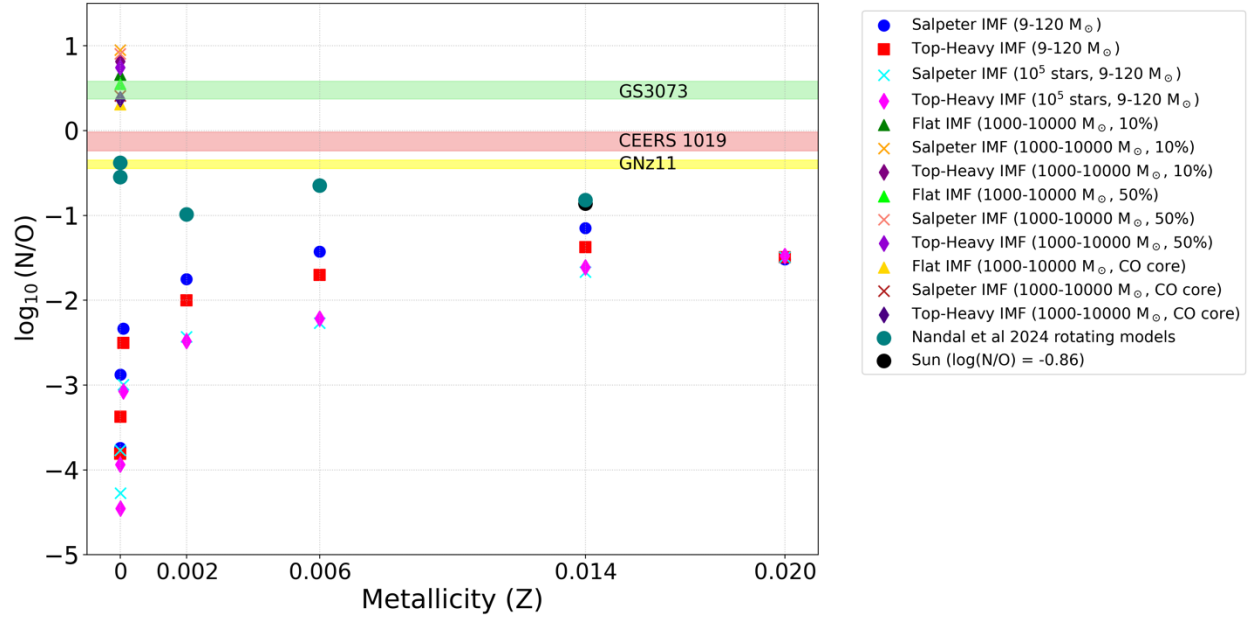


Fig. S5. N/O ratios of 1000 - 10,000 M_{\odot} stars and a variety of 9 – 120 M_{\odot} populations of stars.

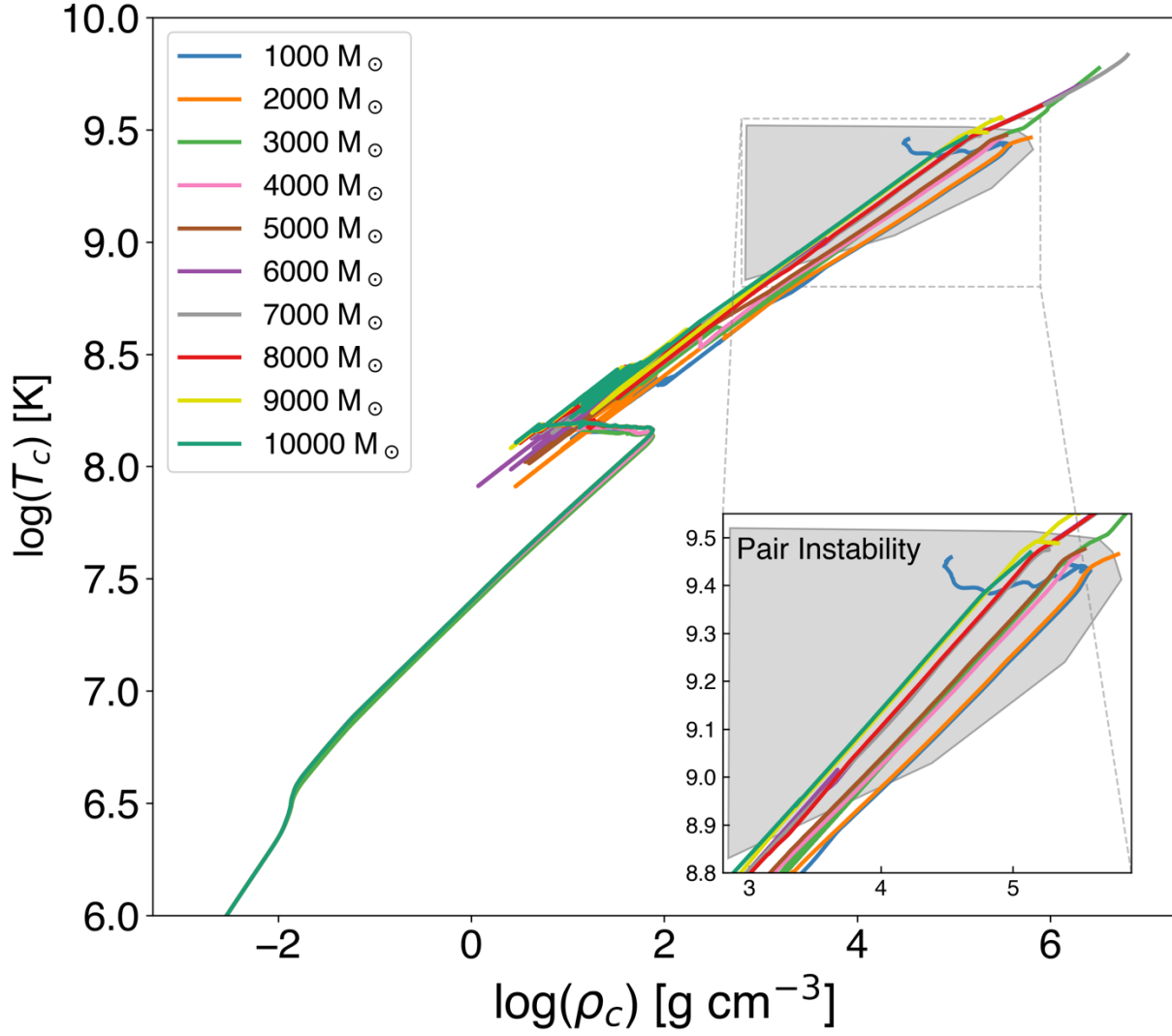


Fig. S6. Evolution of central densities versus central temperatures. The grey shaded zone is the PI regime. A few models such as the 6000, 7000, 8000 M_\odot stars were evolved past the PI into core Si burning.

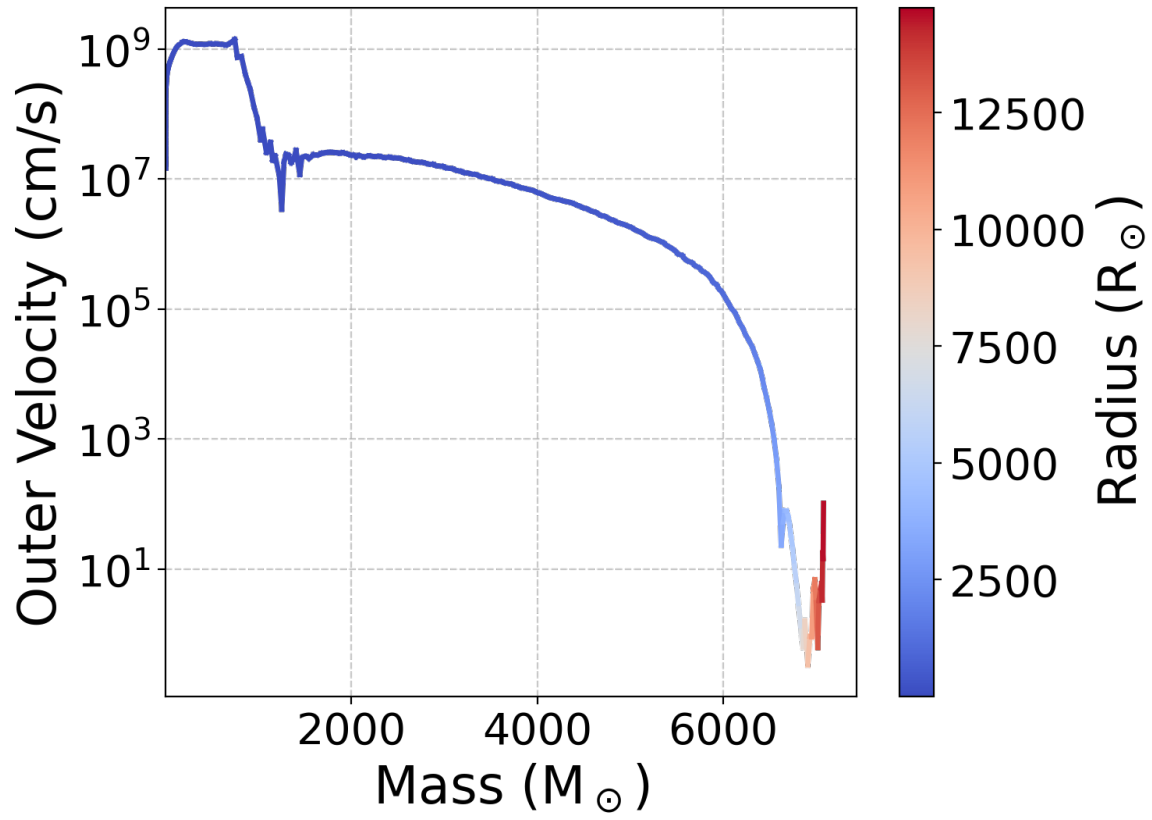


Fig. S7. Collapse of the 8000 M_{\odot} star to a BH.

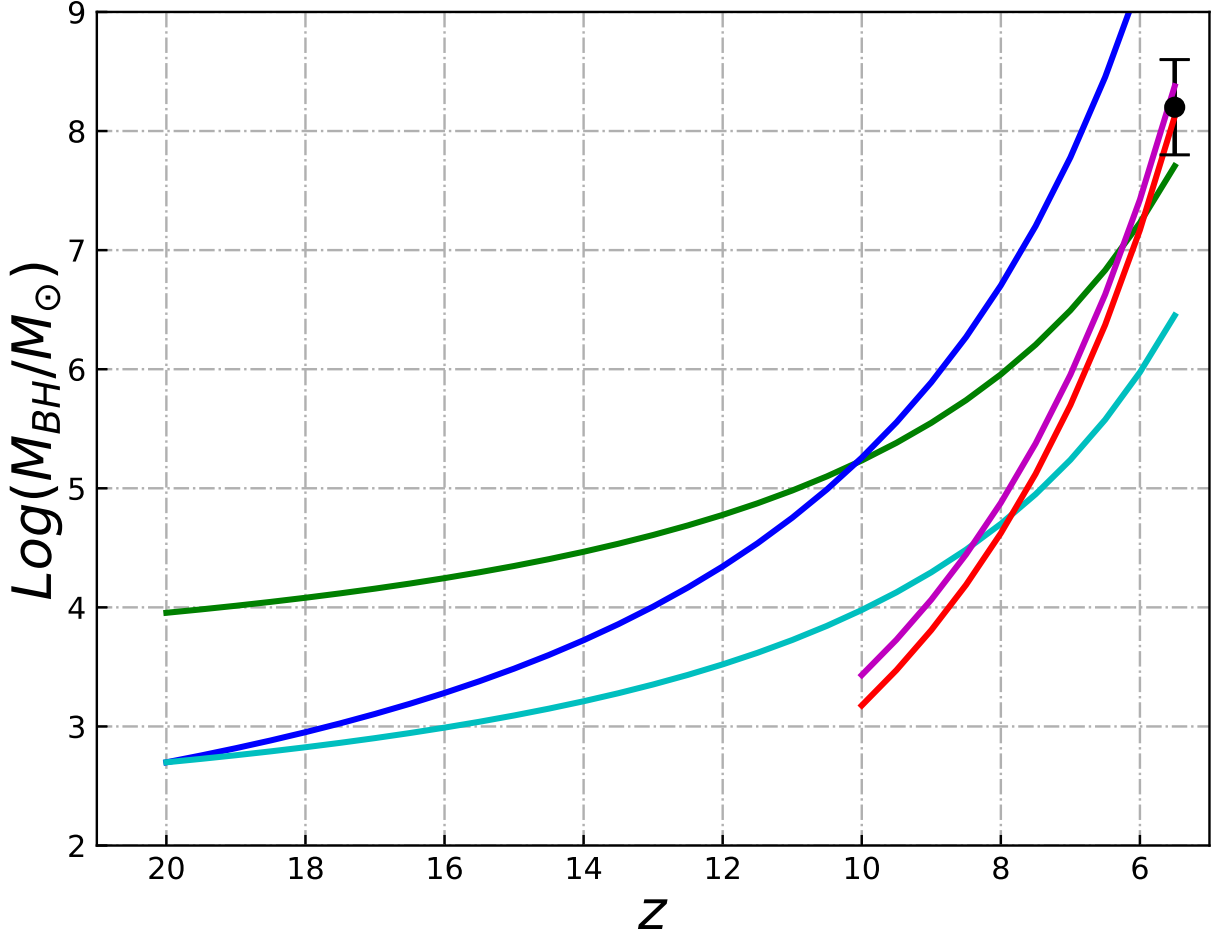


Fig. S8. BH growth rates. Birth redshifts are $z = 10$ and 20 and we consider mass losses of 10% and 50%. The AGN and its error bars in mass are marked by the solid black circle. Green is the $9000 M_{\odot}$ BH growing at $0.5 L_{\text{Edd}}$, blue is the $500 M_{\odot}$ BH growing at L_{Edd} , cyan is the $500 M_{\odot}$ BH growing at $0.5 L_{\text{Edd}}$, magenta is the $2700 M_{\odot}$ BH growing at L_{Edd} and red is the $1500 M_{\odot}$ BH growing at L_{Edd} . Observational constraints on the accretion rate of the AGN at $z = 5.55$ are $0.1 - 1.6 L_{\text{Edd}}$ (16).

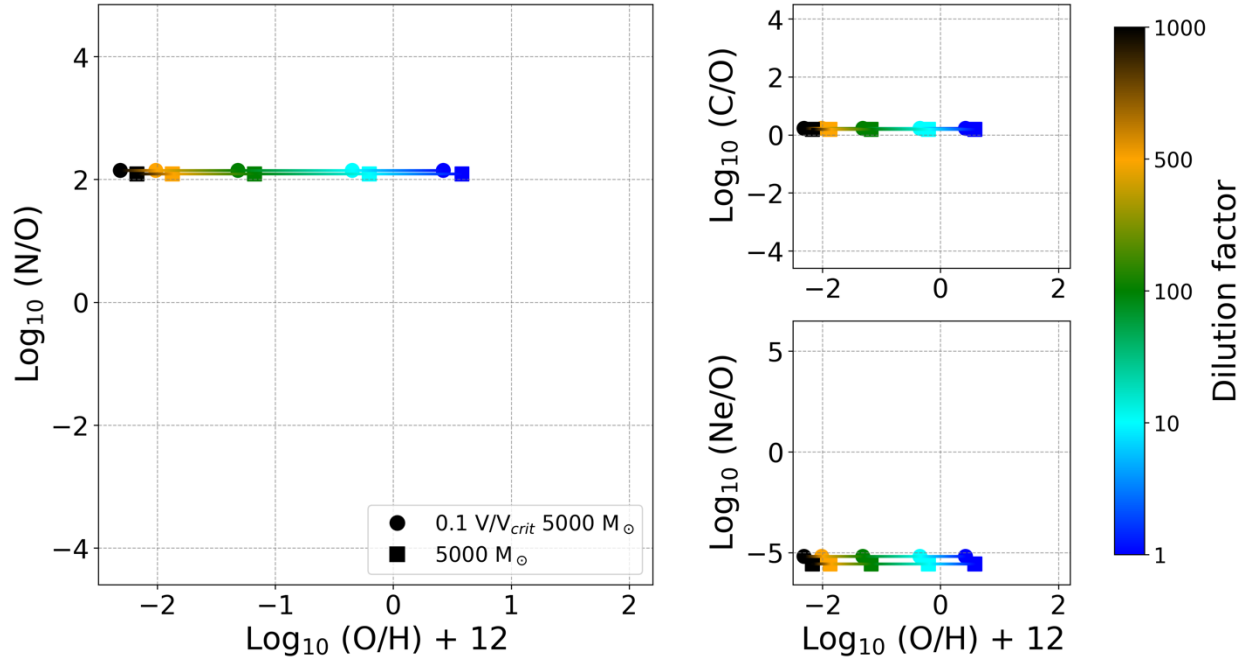


Fig. S9. N/O ratios for rotating and non-rotating stars.

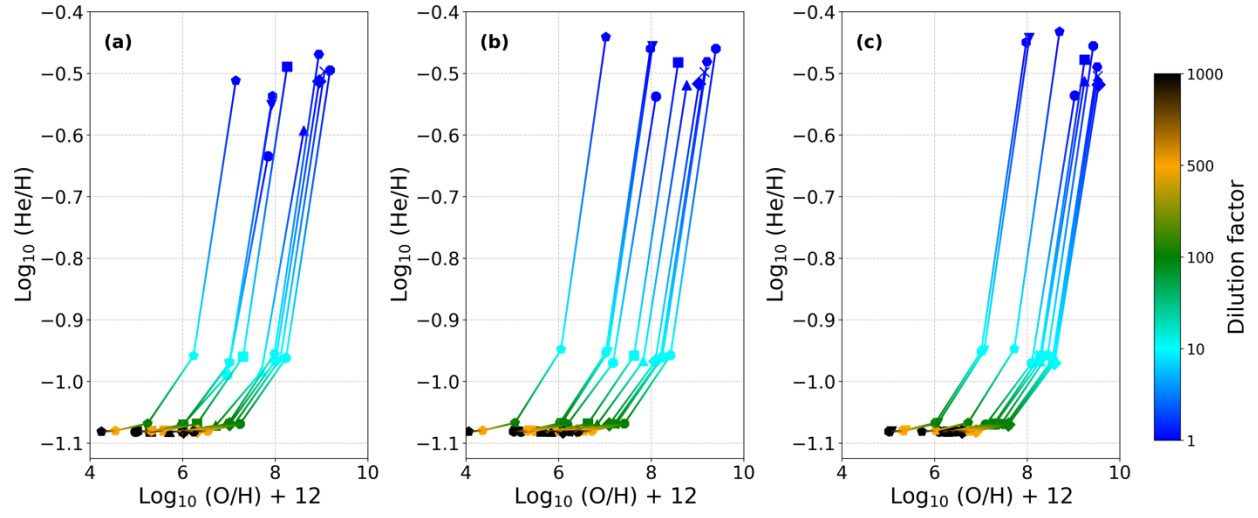


Fig. S10. He/H abundance ratios. Panels a, b and c are for mass losses of 10%, 50%, and the CO core, respectively.

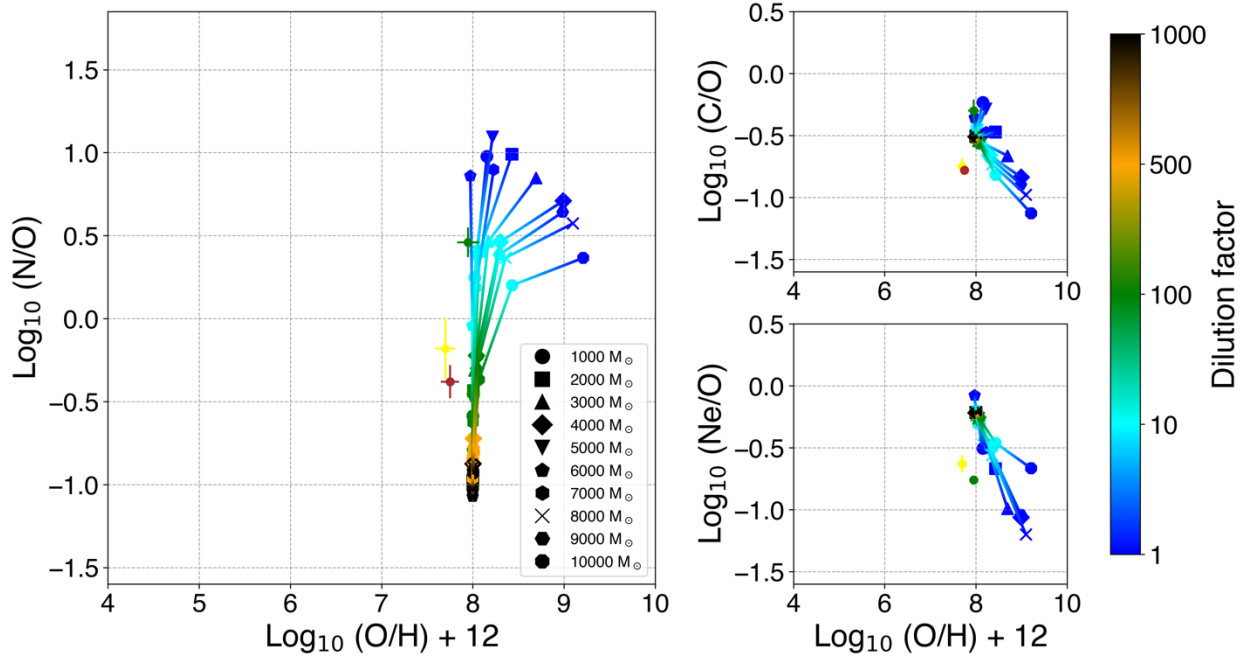


Fig. S11. Abundance ratios of 10 SMSs with contributions by the galactic stars for the case of 10% mass loss. If the chemically mature stellar population contributes C, N, O, and Ne mass fractions $\chi_{\text{C}} = 2.8 \times 10^{-4}$, $\chi_{\text{N}} = 8 \times 10^{-5}$, $\chi_{\text{O}} = 1.2 \times 10^{-3}$ and $\chi_{\text{Ne}} = 9.4 \times 10^{-4}$ then all 10 models can reproduce the observed near vertical transition in N/O ratio in Fig. 4 of Ji *et al.* (2024) while also explaining the C/O ratios.

M _{tot}	M _{cont}	Ej %	M _{ej}	M _{H1}	M _{He4}	M _{C12}	M _{C13}	M _{N14}	M _{O16}	M _{Ne20}	M _{Ne22}
1001	900	10%	101	29.2	70.5	0.07	0.01	1.85	0.11	0	0
2007	1804	10%	203	20.7	174.1	0.13	0.04	6.36	0.5	0	0.01
3026	2724	10%	303	57.8	216.1	0.28	0.07	13.88	1.9	0	0.01
3817	3435	10%	382	46.1	314.1	0.47	0.12	23.45	4.78	0.19	0.03
5238	4713	10%	525	91.5	415.8	0.35	0.08	13.91	0.65	0	0.04
6095	5485	10%	610	114	551.7	0.11	0.03	5.37	0.13	0	0.35
7079	6371	10%	708	120	576.7	0.24	0.06	11.9	0.91	0	0.05
8075	7257	10%	818	80.7	682.8	0.87	0.23	45.68	12.98	0.36	0
9062	8155	10%	907	76.8	804.9	0.87	0.23	45.09	10.68	0.52	0
10024	9021	10%	1003	105	843.7	0.94	0.26	44.45	20.39	4.79	0.13
1001	501	50%	501	80.5	403	0.72	0.11	16.07	0.92	0	0
2007	1004	50%	1003	96.3	870	0.78	0.18	32.15	5.02	0.62	0.06
3026	1528	50%	1498	191	1216	1.73	0.47	93	12.31	0.01	0.07
3817	1909	50%	1908	220	1538	2.45	0.59	115	27.43	2.14	0.15
5238	2620	50%	2618	183	2351	2.08	0.56	91.53	3.67	0	0.51
6095	3047	50%	3048	204	2845	0.72	0.2	34.39	0.42	0	2
7079	3540	50%	3539	274	3177	1.67	0.46	84.7	4.53	0.02	0.33
8075	4038	50%	4037	381	3338	4.82	1.15	225	74.97	5.99	0.02
9062	4531	50%	4531	337	3822	5.62	1.13	217.1	93.42	19.44	0.01
10024	5013	50%	5011	201	4253	6.32	1.75	274.4	158.1	50.13	1.06
1001	298	CO	703	104	561.6	1.64	0.15	22.9	8.5	1.4	0
2007	482	CO	1524	124	1320	2.2	0.28	49.8	28.0	5.88	0.1
3026	867	CO	2159	228	1740	4.14	0.69	138.1	44.4	7.59	0.1
3817	959	CO	2858	262	2224	7.26	0.88	173.5	124.8	28.99	0.23
5238	1205	CO	4033	203	3655	3.27	0.89	145.3	5.8	0	0.87
6095	1619	CO	4475	219	4199	1.85	0.3	51.95	14.8	5.25	2.99
7079	2024	CO	5056	316	4578	2.47	0.68	125.5 ₈	6.3	0.03	0.48
8075	2299	CO	5776	444	4577	13.4	1.63	318	245	61	0.04

9062	2867	CO	6195	385	5020	11.7	1.52	291	249	75.9	0.01
10024	2762	CO	7262	202	6120	9.67	2.67	409	243	80.3	1.66

Table S1. Elemental yields for 1000 - 10,000 M_{\odot} Pop III stars for mass losses of 10%, 50%, above the CO core and complete disruption. All masses are in M_{\odot} . M_{tot} is the final mass of the model at the end of computation, M_{cont} is the mass kept by the star at the time of collapse, and M_{ej} is the mass lost to the ISM.